ADVANCED MATERIALS
www.advmat.de

Self-Sustained, Continuous Jumping of a Light-Driven Electronics-Free Insect-Scale Soft Robot

Wenzhong Yan, Pengju Shi, Zixiao Liu, Yuzhen Chen, Yichen Yan, Yusen Zhao, Chi Chen, David Martinez, Ankur Mehta, and Ximin He**

Insects scavenge energy from the environment for self-sustained operation, and some species use repeated jumping to traverse varied terrain. Such capabilities are desirable for surveillance, disaster recovery, environmental monitoring, and hazardous environment exploration. However, insect-scale (sub-gram) robots are typically limited to few jumps due to inefficient integration of energy, actuators, and control. Here, insect-scale (301 mg) soft robots capable of continuous, autonomous jumping with energy harvesting, actuation, and control embedded in their physical structure without electronics are introduced. Powered by constant light, a single robot achieves 188 nonstop jumps and accumulates over 800 jumps in a year without diminished performance. This behavior is enabled by self-sustained, repeated snapping (SSRS), a light-driven mechanism from a self-shadowing-induced feedback loop based on dynamic light–material interplay. The SSRS exploits snap-through instability and self-shadowing of photoresponsive liquid crystal elastomers (LCEs), enabling untethered, perpetual actuation, and the snapping dynamics are investigated through simulations and experiments. Beyond sustained motion, the robot demonstrates self-righting, directional jumping, obstacle negotiation, hazardous gas sensing, and extreme load-bearing (≈1700 times its weight), highlighting potential for disaster recovery, confined-space exploration, and environmental monitoring. This work advances insect-scale robotics toward fully autonomous, long-lived micro-robots.

1. Introduction

Insects are adaptable and agile creatures that demonstrate remarkable locomotion and sensory processing that allow them to navigate complex environments with ease.[1] Despite their vastly varied kinematic and biological mechanisms, jumping is one of the most common locomotion modes that enables insects, e.g., springtails, grasshoppers, and click beetles, to survive in diverse environments.[2] Jumping helps them navigate unstructured and complex habitats, escape from predators, efficiently capture prey, conserve energy during long-distance travel, and more. Most importantly, insects' capability of scavenging energy from environment allows long-term, continuous jumping. These remarkable capabilities thus have inspired numerous insect-scale (subgram) robots.[3] Their small size and mass inherently lower their inertia, making them more resilient in launching, landing, or colliding with obstacles.[4] In addition, the realization of man-made insect-sized analogues with similar levels of performance could significantly facilitate the deployment of robots in harsh environments for meaningful tasks. For example, these robots could be used to navigate tight spaces that are inaccessible to people or large mobile robots for applications such as critical infrastructure inspection, search and rescue after natural disasters, or environment monitoring.[5]

There have been increasing efforts toward this goal of autonomous and self-sustainable insect-scale robots that can continuously jump. This usually requires a power system that can continuously supply energy to sustain long-term operation,[6–8] actuation that rapidly releases a huge amount of energy (with or without power amplifying mechanisms),[4,9,10] and control that regulates energy harvesting, actuation, launching, landing, and self-righting for continuous jumps.[11–13] Furthermore, those three classes of components must form an ecosystem that

W. Yan, A. Mehta
Electrical and Computer Engineering Department
University of California Los Angeles
Los Angeles 90095, USA
E-mail: mehtank@ucla.edu
W. Yan
Mechanical and Aerospace Engineering Department
University of California Davis
Davis 95616, USA

The ORCID identification number(s) for the author(s) of this article can be found under https://doi.org/10.1002/adma.202519669

DOI: 10.1002/adma.202519669

P. Shi, Z. Liu, Y. Yan, Y. Zhao, C. Chen, X. He
Materials Science and Engineering Department
University of California Los Angeles
Los Angeles 90095, USA
E-mail: ximinhe@ucla.edu
Y. Chen, D. Martinez
Mechanical and Aerospace Engineering Department
University of California Los Angeles
Los Angeles 90095, USA
X. He
California Nanosystems Institute
University of California Los Angeles
Los Angeles 90095, USA

accommodates both signal and energy transduction. Such integration requires closed-loop coordination between sensing, energy conversion, and mechanical response. These components are relatively easier to be integrated in large-scale agents[14–17]; miniaturization of such systems into sub-gram scale is nontrivial.[18] A few components and some of their assemblies have been demonstrated individually.[10,19–23] Nevertheless, it is still very challenging to build such small-scale robotic systems in large part due to the lack of integrated design and fabrication strategies that enable long-term, robust autonomous impulsive operation.[3,24]

Recent advances in stimuli-responsive materials provide a promising route to achieve untethered, autonomous jumping systems with integrated power, actuation, and control components.[25,26] Stimuli-responsive materials can change shape and properties (e.g., color, stiffness) in response to environmental cues, providing the potential to achieve functions including self-powering, self-actuation, and self-regulation.[27–32] In particular, photo-responsive liquid crystalline elastomer (LCE) exhibits large, anisotropic, and reversible actuation triggered by light.[33] This optically controlled actuation can be harnessed to generate autonomous motion including self-sustained flapping, rolling, and crawling.[34–37] However, few of these materials and mechanisms are applicable to create autonomous soft jumping robots, potentially due to their limited actuation speed and thus low power density to initiate impulsive motion.[38]

To increase power density of stimuli-responsive materials for impulsive motions, latch-mediated mechanisms – composed of springs and latches – are often incorporated.[39–43] Buckling instability constitutes a special class of latch-mediated mechanism that leverages the internal constraint of a snap-through transition as a geometric latch without requiring additional components.[44–48] Small-scale jumping robots can benefit from the high efficiency in both space and weight combined with good controllability of buckling instability to simplify design, reduce mass, and eliminate small delicate parts beyond the limit of current fabrication and materials.[49] However, most machines are restricted to a limited number (if not one) of jumps due to the lack of resetting mechanisms to autonomously regulate power and position after each jump,[4,50–53] which inhibits their practical applications (see Figure S1 and Table S1, Supporting Information; for the taxonomy of jumping robots). Recently, Kim et al. had reported an autonomously snapping and jumping gel utilizing volume change associated with solvent evaporation.[52] These devices would stop jumping when the solvent depletes. Meanwhile, other soft jumping robots that claim to perform continuous jumping would still require manual manipulation of external stimuli.[42,54] The jumping height of these robots is impressive; however, a genuinely self-sustained device that performs long-duration, autonomous jumps is still rare (see Figure S1 and Table S1, Supporting Information for detailed taxonomy of jumping robots). While light-powered LCE films and torus have demonstrated self-continuous jumping powered by light,[55,56] a fully autonomous, payload-capable soft robot has yet to be developed.

Here, we report fully autonomous insect-scale soft robots capable of continuous jumping with energy harvested from the environment, functionally analogous to their biological counterparts (**Figure 1**A,B). Noting that we are not directly mimicking the jumping mechanism of grasshoppers. Despite its jumping height (≈1.6 times body height) being not among the most high-performing jumping robots, this work remains one of the few examples of a soft robot achieving autonomous, continuous jumps without manual intervention (Figure S1, Supporting Information). Uniquely, we achieve this by embedding energy harvesting, actuation, and control into the physical structure of the robot without relying on electronics. Specifically, a robot shows 188 times continuous jumps (Movie S1, Supporting Information) and can execute over 800 jumps collectively in the span of a year, with well-retained stable performance (i.e., height and period) without noticeable degradation.

These jumping robots are mainly enabled by a self-sustained, repeated snapping (SSRS) mechanism that exhibits perpetual and untethered high-power motions, fueled remotely by constant visible light (Figure 1). The SSRS derives from a self-shadowing-induced built-in feedback loop based on the dynamic light–material interplay.[34,57–61] Specifically, light irradiation photothermally heats the LCE, and the local heating induces LCE contraction, which triggers snapping. The LCE configuration upon snap-through closes the shutters, which blocks the light to allow cooling and relaxation of LCE, thereby reopening the shutters with a snap-back. This interplay leads to cyclic snapping to allow continuous, repeated rapid motion.[34,58,59] Critically, the SSRS mechanism embodies a form of physical intelligence, wherein the geometric design, material response, and energy transduction are intrinsically coupled to autonomously regulate the jump cycle without electronics or programmed control.[26,62] Such intelligence governing actuation and reset is embedded directly into the physical structure and its interaction with light, resulting in a fully mechanical decision-making process driven by environmental input. We show that a fixed SSRS device can perform over 500 snap-through and snap-back cycles with negligible performance degradation (Figure S2 and Movie S2, Supporting Information); the maximum cycle number documented is ~30 000 with a shallow SSRS device (Movie S3, Supporting Information). A design principle was established by incorporating finite element simulation and experimental characterization to elucidate the complex dynamics of its photo-thermal-mechanical process and to guide the optimization of specific output energy and power for jumping.

We demonstrate that the SSRS can be utilized to create sub-gram soft robots that are capable of continuous jumps by incorporating the functionality of self-righting using a balancer. With the control of take-off angle, these robots are also capable of directional jumping to locomote over a distance, overcome obstacles, and behave as a platform for hazardous gas detection when equipped with on-board sensors. We also show that these robots have high robustness. After withstanding the weight of a 500 gram mass (~1700 times heavier than the robot), the system survived after removing the mass and continued to function without compromising its jumping performance. In addition, we found that our robots are capable of self-cleaning and jumping under concentrated sunlight. Our work establishes a clear path toward the realization of entirely autonomous, self-sustained jumping robots, akin to insects.

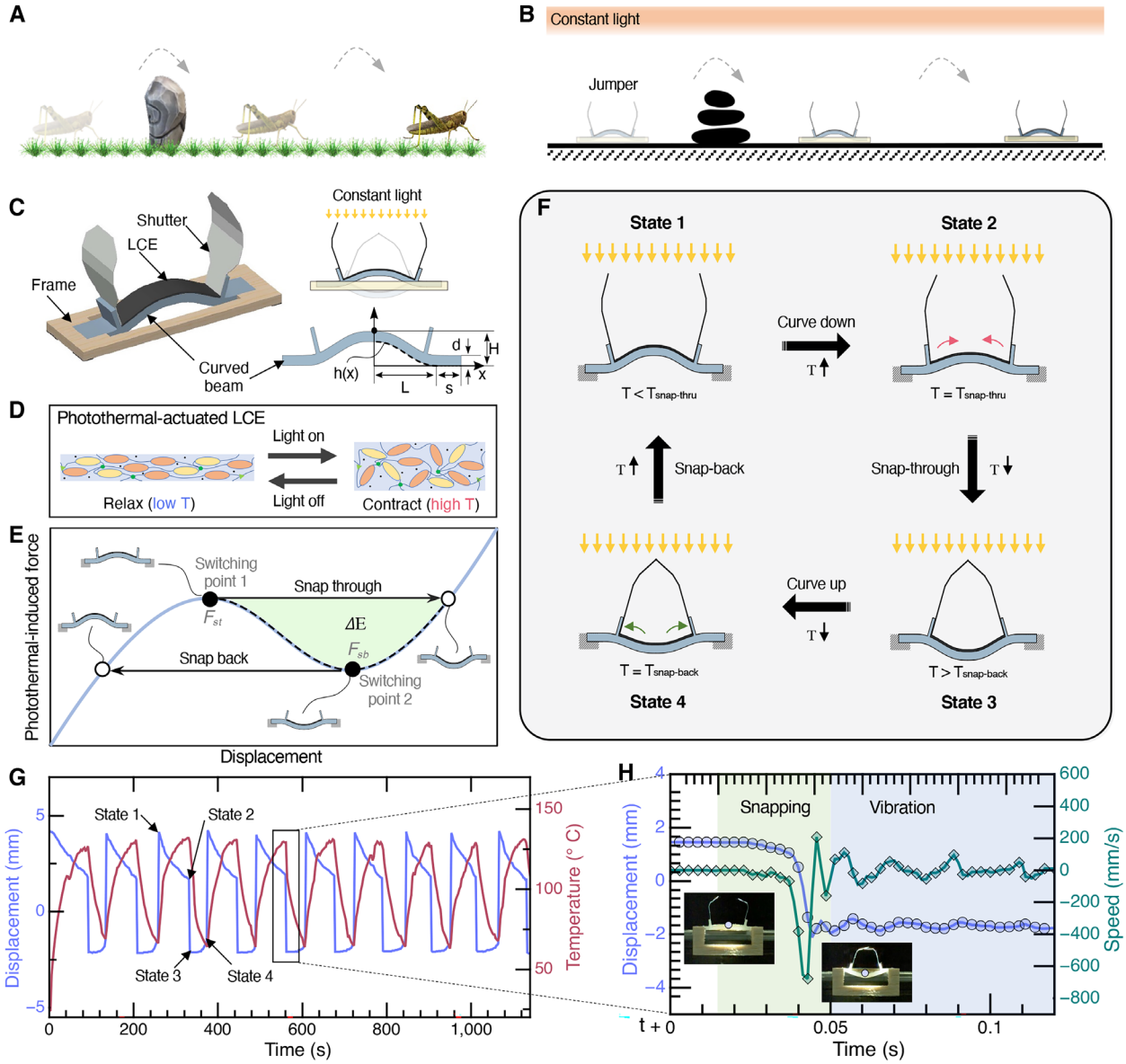

Figure 1. Self-sustained insect-scale robots capable of continuous jumping based on SSRS. A) As an example, grasshoppers use repeated jumps to locomote and overcome obstacles with energy scavenged from the environment. B) Analogously, our robots are capable of continuous jumps with energy harvested from constant light. C) A SSRS is mainly composed of a LCE strip, a curved elastomer beam (with its two ends fixed on a wood frame), and two shutters. The geometry of the curved beam is defined in Equation 1. D) LCE undergoes reversible photothermal actuation. E) Schematic force-displacement diagram for a monostable LCE/curved beam composite. When the (photo)thermal-induced force of the LCE (along the contraction direction) reaches a critical value F_{st}, the beam snaps to the downward position, which leads to a sudden release of energy ΔE (highlighted in green). When the force decreases below the snap-back force (F_{sb}), the beam snaps back to the upward position. F) Working principle of the SSRS mechanism. The shutters control the exposure of the LCE to irradiation, which, when combined with the monostable composite, generates a self-shadowing-enabled built-in feedback loop for cyclic snapping. G) Representative displacement and temperature of the apex of the composite curved beam during multiple cycles of a SSRS device. H) Zoom-in on the displacement curve highlighting the dynamics of one snapping event in (G). The maximum speed of the apex can reach about 680 mm s^{-1}. Vibration of the beam was observed after a snapping event.

2. Results

2.1. Design of Self-Sustained, Repeated Snapping

The SSRS device consists mainly of a photoresponsive actuator (made of LCE), a curved elastomer beam (with its two ends clamped onto a frame), and two shutters (Figure 1C). The LCE strip is attached on the top of the elastomer beam (Dragon Skin 30) using a high temperature glue with high adhesion strength (Figure S3, Supporting Information) to form a LCE/curved beam composite to introduce mechanical instability. The LCE strip has three functions as follows. First, it harvests optical energy from an environmental light source. Second, it contributes to the mechanical instability as a structural component in the

composite beam. Third, it serves as a thermal actuator that drives the movement of the LCE/curved beam composite. It is highly desirable that the LCE has a modulus comparable to that of the elastomer beam to prevent interfacial failure due to stiffness mismatch[15] and can efficiently actuate with a large actuation stroke by photothermal heating. To this end, we synthesized thin LCE (~130 μm) via thiol–ene chemistry by modifying a previously reported method (see Experimental Section; Figures S4 and S5, Supporting Information).[63] Dynamic mechanical analysis shows that the storage modulus of the LCE is 8.8 MPa at 30 °C and reaches a minimum of 1.7 MPa at the temperature of 91 °C (Figure S6, Supporting Information), indicating matching storage modulus with Dragon Skin 30 within one order of magnitude (Figure S7, Supporting Information). The LCE shows a large actuation strain of 33% at a relatively low temperature (~110 °C, Figure S8, Supporting Information), owing to its low isotropic-to-nematic transition temperature (T_{ni}) of 31 °C characterized via differential scanning calorimetry (Figure S9, Supporting Information). Candle soot (CS) was doped into the LCE as a high-performance photothermal agent with good compatibility with the LCE matrix,[64] leading to high absorbance in the visible to near infrared (NIR) range (Figure S10, Supporting Information) and rapid temperature rise under simulated sunlight (Figure S11, Supporting Information). As a result, the LCE can efficiently perform fast actuation when exposed to light (Figure 1D; Figure S12, Supporting Information).

The elastic beam should have minimal thermal expansion and stable thermomechanical properties at elevated temperatures. Herein, we used Dragon Skin 30 (Figures S13 and S7, Supporting Information). The geometry of the curved beam is crucial to creating mechanical instability in the SSRS mechanism. Here we obtained the curved beam by mirroring and then extruding the height profile[65] (see black dashed line in Figure 1C) to a certain width, w:

$$h(x) = \begin{cases} (H-d)\left[1-10\left(\frac{x}{L}\right)^3+15\left(\frac{x}{L}\right)^4-6\left(\frac{x}{L}\right)^5\right], & x \in \{0, L\} \\ 0, & x \in \{L, L+s\} \end{cases} \quad (1)$$

where H is the overall height, d is the nominal thickness, and L is the span of the arc. s denotes the length of the flat portion added at the base of the beam to facilitate the enforcement of clamped-clamped boundary conditions when integrated into a frame. The final beam geometry, shown in Figure 1C, is obtained by offsetting the height profile $h(x)$ by a distance to allow the uniform thickness d (see Text S1 and Figure S14, Supporting Information for detailed geometry).

We fixed the two ends of the LCE/curved beam composite onto a Balsa wood frame to realize a clamped-clamped boundary condition. The Balsa wood frame was selected due to its high specific stiffness and small thermal expansion.[66,67] The assembled structure is monostable with a snap-through transition (Figure 1E). When subjected to a sufficient thermally induced force (causing the beam to pass the switching point) from the LCE, the beam can snap into a concave shape (unstable state), yielding a displacement at its center. During this snapthrough process, the beam rapidly releases its kinetic energy (ΔE, the enclosed green area). When the thermally induced force decreases, the beam goes back through the switching point and snaps back to its stable state.

Combined with shutters, the fabricated device can generate self-repeating snapping. Two shutters are bounded on the composite beam to passively control its exposure to light. We used aluminum vapor-coated polyethylene terephthalate (PET) as the material for the shutters to efficiently reflect visible light used for photothermal actuation. Figure 1F shows the working principle of the SSRS mechanism, based on the built-in feedback loop strategy, previously demonstrated in various self-regulated functions[27,59–61] and diverse motion modes such as light tracking[57] and oscillation.[58] Also, the shutter design enables actuation powered by an overhead light source similar to sunlight.[34] Initially, the system rests at State 1. Once exposed to light, the LCE is photothermally heated and contracts anisotropically along the length to generate smooth bending in LCE/curved beam composite (State 2). Upon reaching a critical contracting force F_{st}, the composite beam undergoes an abrupt snap-through buckling transition, releasing kinetic energy within a short time, which is critical for driving impulsive motion. The snap-through buckling closes the shutters and thus introduces a shadow to block the incoming light (State 3). This self-shadowing mechanism causes the cooling and relaxation of the LCE, gradually reversing the bending of the composite (State 4). Further relaxation would initiate a transient snap-back, opening the shutters, and resetting the system to its original state (State 1). The geometry, position, and orientation of the shutters were empirically optimized to minimize the blockage of light before snap-through while guaranteeing full shadowing after snapping (the same optimization applies for the snap-back process).

We placed a SSRS device under a constant light with intensity of 792 mW cm^{-2}, generated by a solar simulator (see Table S2, Supporting Information; for the SSRS device's detailed parameters). The composite beam started to undergo transient snapping events as designed. We recorded both the movement and temperature of the apex of the beam (Figure 1G, Figure S15, Supporting Information). The cyclic snapping motion of the beam occurred at the same frequency as its temperature fluctuation with a phase difference of about 180°, which supports the formation of a photo-thermo-mechanical built-in feedback loop intrinsic to the light-material interactions. The peak snapping speed of the apex of the composite was ~680 mm s^{-1} with an average speed of about 10 mm s^{-1} (Figure 1H). These extraordinarily fast apex speeds occur at discrete moments (each lasting ~11 ms) and comprise a small fraction of the observed movements. The resetting (from State 3 to State 1, passing State 4) involves a similar process: a slow unbending of the composite beam followed by an abrupt snap-back (Movie S4, Supporting Information). This snap-through instability provides a powerful amplifying mechanism that decouples the slow actuation from the output deformation and triggers rapid events, useful for driving impulsive motion with slow actuators. Meanwhile, the self-shadowing effect autonomously regulates the onset and reset of snapping events. In summary, our SSRS mechanism, combining snap-through instability and self-shadowing, provides a new way to generate self-sustained high-power autonomous motion.

To obtain a deeper understanding of the snap-through process, we used finite element analysis to simulate a SSRS device with dimensions of H = 4 mm and d = 1.5 mm (see Text S2, Movie S5, Supporting Information). **Figure 2A** shows a side-by-side comparison of experimental and simulated deformations at

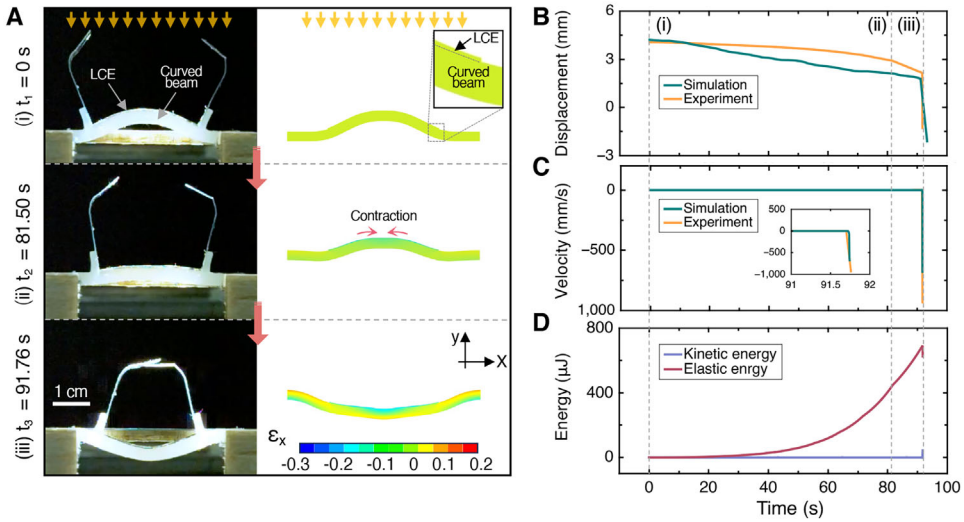

Figure 2. Photo-thermal-mechanical FEA of snap-through buckling. A) A side-by-side comparison of experimental and simulated deformations at three instances during a cycle (Left: snapshots of the SSRS device. Incident light impinges directly from the top of the device; Right: frames of strain distribution from FEA along x-direction. The boundary constraint is not shown here). B) Correlation of measured and simulated displacement of the device's apex during a snapping event. C) Comparison between experimental data and simulation of velocity curves for the apex of the beam, with a detailed zoom-in on the snapping event presented in the insert. D) The evolution of the elastic energy and kinetic energy of the device (including LCE and curved elastomer beam) throughout the snap-through process.

three key moments during the snap-through buckling, suggesting a good agreement with each other. It is observed that the contracting strain along the *x*-direction peaks in the middle top of the beam, attributed to the greater light intensity received at the center due to its curved shape and consequently larger actuation force (Figure S15, Supporting Information). The displacement and velocity of the apex of the composite beam were further extracted and plotted in Figure 2B,C, respectively, showing similar consistency with experimental results. We also analyzed the evolution of the stored elastic energy and kinetic energy of the device over time (Figure 2D). Upon irradiation, the LCE absorbed photon energy and converted it into thermal contraction to cause the overall deformation of the device. The deformation induced elastic energy accumulation until it reached the critical point for the onset of snap-through buckling (~91.8 s), resulting in a drop of 67.7 μJ. This energy release was subsequently converted into kinetic energy due to mechanical instability. The kinetic energy remained a very low value due to the slow deformation before the onset of snap-through until a rapid jump, reaching ~50.7 μJ. This value is comparable to the experimental measurement of the kinetic energy of about 55.7 ± 1.8 μJ (further discussed in the next section). In addition, simulation results suggest that LCE with lower T_{ni} and larger actuation strain yields snap-through motion with greater kinetic energy (Text S2, Figure S16, Supporting Information). In summary, the comparisons validate that the FEA model can effectively capture the device behavior. For a precise assessment of the device's performance, additional experimental validation is required, as detailed in the subsequent section.

2.2. Controlling the Snapping Dynamics

Aimed at powering robots for rapid motions, the specific energy and specific power during the snapping events of the SSRS mechanism are of great importance.[4] The geometry and material properties of the composite beam influence the snapping behavior. Simulation results show that a beam with higher storage modulus leads to larger maximum kinetic energy reached during the snap-through, while the viscoelasticity has minimal effect on the deformation dynamics of the beam (Figure S17, Supporting Information). Therefore, we selected Dragon Skin 30 as an elastomer that is relatively stiff to improve the power output, while still being soft enough to be actuated by the LCE (Text S3, Supporting Information). Based on the selected materials of the LCE and the curved beam, we then investigate the effect of geometry on specific energy and specific power. Owing to complex material composition, geometry, and multi-physics interaction, it is impractical to use analytical and numerical methods to investigate the effects of the device's geometric design parameters on dynamic performances. Instead, we used experimental methods. To fabricate subgram devices and robots, we set the span L of the arc to be 10.0 mm. The thickness of the LCE was fixed as 130 μm for all tests for ease of fabrication while ensuring sufficient penetration depth for light absorption (Figure S10, Supporting Information). The width w of the curved beam was also kept constant as 4.0 mm, due to its independence on the mechanical properties. Thus, the normalized height $\bar{H}(= H/L)$ and the normalized thickness $\bar{d}(= d/L)$ of the curved beam were identified as the primary controlling parameters. The experiments were carried out by changing these design parameters while keeping all others constant.

These design parameters influence the relationship between the input light intensity and the released energy during a SSRS snap-through event (see Text S4, Supporting Information; for how to measure specific released energy). As shown in **Figure 3**A, when the light intensity is low, the beam only underwent smooth bending deformations, without snapping to the inversely curved

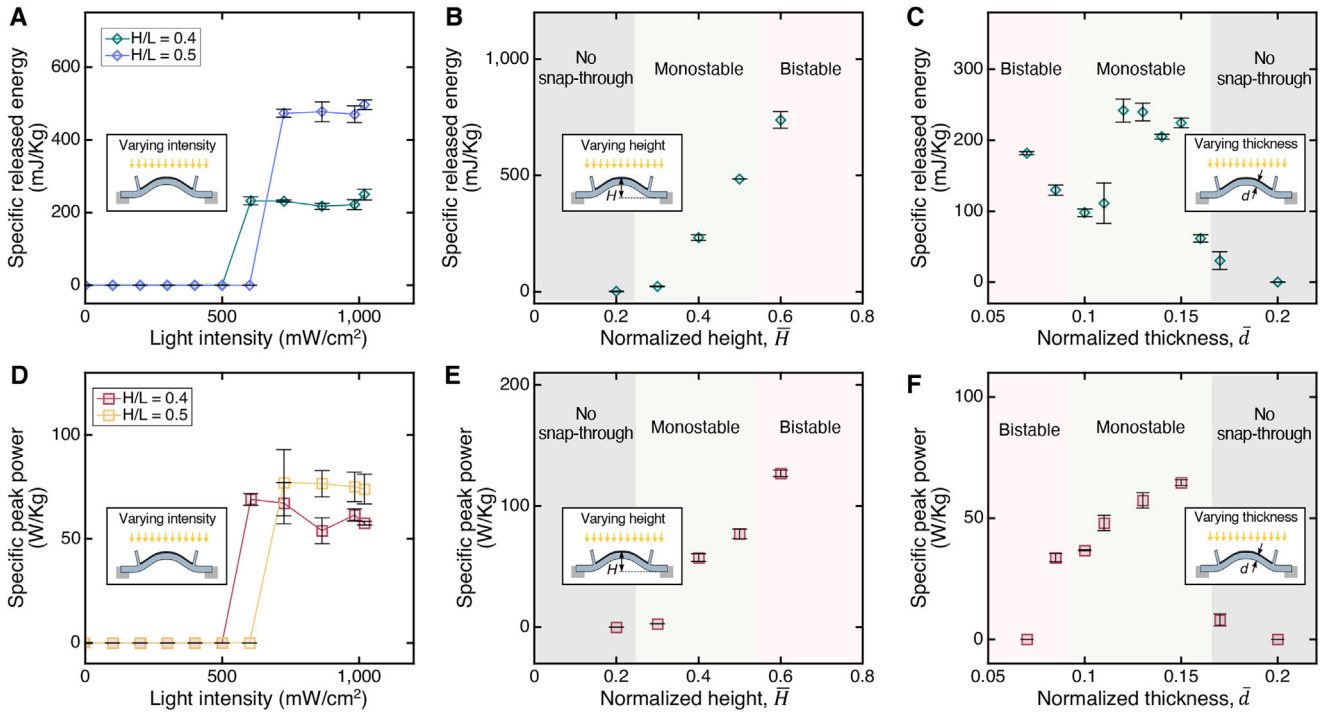

Figure 3. Influence of input power and geometrical parameters on released energy and output power. (A-C) Specific released energy as a function of light intensity I (d = 1.3 mm, H = 4.0 mm or 5.0 mm), normalized height $\bar{H}$ (d = 1.3 mm, I = 1020 mW cm^{-2}), and normalized thickness $\bar{d}$ (H = 4.0 mm, I = 1020 mW cm^{-2}), respectively. (D-F) Specific peak power as a function of light intensity I (d = 1.3 mm, H = 4.0 mm or 5.0 mm), normalized height $\bar{H}$ (d = 1.3 mm, I = 1020 mW cm^{-2}), and normalized thickness $\bar{d}$ (H = 4.0 mm, I = 1020 mW cm^{-2}), respectively. The error bars represent the standard deviations of the values obtained from three different measurements. $\bar{H} = H/L$ and $\bar{d} = d/L$. Beams in light gray shade in (B, C, E, and F) do not show snap-through behaviors.

structure. Once the intensity reached a critical value, the beam started to generate snap-through transitions, releasing a certain amount of energy. Note that the released energy was minimally affected by the magnitude of the incident light density above the critical value due to the structural instability of the composite curved beam, which intrinsically decouples the energy output from its input's dynamics. In the case of $\bar{H} = 0.4$, the critical light intensity is about 605 mW cm^{-2} with a specific released energy of ≈232 mJ kg^{-1}. When $\bar{H}$ increases to 0.5, the critical intensity increased to approximately 726 mW cm^{-2} with a higher released energy of about 480 mJ kg^{-1}. This increase in the critical light intensity is mainly caused by the beam's raised energy barrier (the switching point 1 moving up in Figure 1E).[65]

By varying the beam height H, we further discovered that the response of the beam underwent several transitions (Figure 3B). For low values of $\bar{H}$ (i.e., for shallow beams), the device does not exhibit transient snapping (light gray region). By increasing $\bar{H}$, snapping is eventually triggered upon radiation. Within a certain domain (light green region), the beam was able to snap back to its original shape after removal of light, exhibiting monostability that are desired for our SSRS mechanism. The specific released energy increases monotonically as a function of $\bar{H}$, suggesting that the response of our beam can be enhanced using sufficiently deep configuration. However, for higher values of $\bar{H}$, the beam becomes bistable and fails to snap back to its original state after removing the light, preventing cyclic snapping events (light pink region). Overall, the released energy increases monotonically with height.

The relationship between beam thickness and specific released energy is more complex, arising from the change in beam mass and transition of instability state (Figure 3C). For small thicknesses, the beam is bistable and does not spontaneously snap back, with specific released energy monotonically decreasing as a function of $\bar{d}$ (light pink region); this is primarily due to the larger mass of the beam at increasing thickness. Upon further increasing the thickness, the device transitioned into a monostable state. The specific released energy reached its maximum (≈240 mJ kg^{-1}) with an appropriate thickness (i.e., $\bar{d}$ = 0.13 in Figure 3C in the light green region) and remained relatively stable up to $\bar{d}$ = 0.15. For a typical composite beam with mass of ≈200 mg, the released energy is 55.7 ± 1.8 μJ, which agrees well with the simulation result of kinetic energy that increased during the snap-through process (50.7 μJ, Figure 2A). When the thickness was further increased, the beam exhibited no snap-through instability, leading to a drastic drop in released energy. Such trend is also supported by FEA simulations (Text S2, Figure S18, Supporting Information), revealing the complex nonlinear coupling between beam geometry and energy output. In general, an appropriate combination of thickness and height needs to be carefully

chosen to ensure the occurrence of self-repeating snapping with high specific released energy.

In addition, we experimentally characterized the influence of incident light intensity I, normalized height $\bar{H}$, and normalized thickness $\bar{d}$ on the specific peak output power of the SSRS device (see Text S5, Supporting Information; for how to measure specific output power). As shown in Figure 3 from D to F, the specific peak power presents a similar dependence on the three design parameters to that for the released energy. This positive correlation is favorable for the optimization of the SSRS systems since it is desirable to have both large released energy and high output power for driving impulsive motions. Specifically, the peak power density was found to reach an upper limit (≈ 99 W kg^{-1}) at a design with its height and thickness of 5.0 and 1.3 mm, respectively. This value is comparable to the power density of some insects that jump via a latch-mediated mechanism, e.g., the desert locust *Schistocerca gregaria* (~18 W kg^{-1}, normalized against whole body mass).[68]

2.3. Autonomous, Untethered Continuous Jumping

Investigation of repeated, transient snapping of the SSRS devices suggests that an appropriate design could facilitate autonomous, continuous impulsive motion. Based on this concept, we created an insect-scale jumping robot, which could harness the cyclic, fast transitions of the beam to realize autonomous continuous jumping, powered remotely by a constant visible light source. The working principle of the robot is depicted in **Figure 4A**. Once a constant light is supplied (from the top), the composite beam snaps through with its curvature inverted to hit the ground, which generates a force to launch the robot into air. After landing, the cooled beam eventually snaps back to its original state. Thus, the robot can achieve continuous snapping-based jumps without the need for control or external input. Notably, the jumping robot is untethered and does not require physical connections to power sources.

To enable repetitive jumps, it is necessary to incorporate self-righting—resetting the orientation of the robot—to prepare it for consecutive launching. For insect-scale robots, we must realize such self-righting in a space and mass-efficient manner.[69] We also want to keep the mechanisms as simple as possible to ease the manufacturing and assembly process. To satisfy the above two requirements, we decided to use a passive self-righting mechanism. Onto the wooden frame of the SSRS device (see Table S3, Supporting Information for its detailed parameters), we mounted two carbon fiber filaments as balancers (Figure 4B, ~301 mg). This simple design of the jumper can effectively achieve self-righting (Figure 4C). These balancers add negligible mass to the jumper, leaving the monostable beam with ≈70% of the weight of the complete robot (see Table S4, Supporting Information). Meanwhile, after the robot launches, the beam stays in the downward (inverted) position. The resulting distribution of mass stabilizes the orientation of the robot during flight toward a predictable upright landing.[10] The added balancers enlarge the landing base to prevent the robot from tipping or rolling after landing (observed in Figure 4D,E; Movie S6, Supporting Information). Thus, after landing, the robot is oriented appropriately for the next jump. Using this self-righting strategy, we could achieve autonomous, untethered continuous jumping under constant light irradiation of 984 mW cm^{-2} (Figure 4F, Movie S7).

This jumping motion was primarily directed along the vertical axis with small, randomly directed horizontal displacements (Figure 4F, bottom). This pattern is driven by the transition mode of the monostable beam during the snapping events; our designed monostable beam (H = 4.0 mm, d = 1.3 mm) features a symmetric transition mode (in orange, Figure 4G). This generates an actuation force perpendicular to the ground, leading to a vertical launch (Figure 4D, Movie S8, Supporting Information). By using a deeper beam (H = 5.0 mm, d = 1.3 mm), the energetically favored[59,70] transition mode becomes asymmetric with an S-shape (orange curve in Figure 4H, Movie S9, Supporting Information). In general, thicker and shallower beams are more likely to exhibit symmetric U-shaped snap through, while thinner and deeper beams tend to favor asymmetric S-shaped transitions (Figure S19, Supporting Information). The resulting snap-through transitions impart a predictable off-axis impulse adding a horizontal component to the jump (Figure 4I). This autonomous, untethered robot can repeatedly jump in a single direction (Figure 4J, Movie S10, Supporting Information) with a height of about 40 mm and a horizontal distance of approximately 25 mm per jump (Figure 4K). The horizontal motion of the robot requires more robust self-righting. We devised a complementary passive mechanism to keep the robot's center of gravity located in the lower part of the structure and create a roll moment to upright itself (Text S6, Movie S11, Supporting Information). This mechanism adds weight to the frame, reducing the energy of each jump in order to ensure repeated performance. A comparison of jumping performance with reported jumpers is detailed in Figure S1 and Table S1 (Supporting Information).

2.4. Functional Capabilities and Robustness

When faced with rugged terrain, insect-scale robots must be able to negotiate obstacles during locomotion. Our jumper can leap over a hurdle of 26 mm (≈1.6× body height) and continue jumping along the same direction afterward (**Figure 5A**, Movie S12, Supporting Information), maintaining excellent mobility over uneven surfaces. Furthermore, the combination of the soft LCE/Dragon Skin actuator and the flat wooden frame endows our jumper with a high mechanical robustness. We applied a load of 500 g (approximately 1700× body weight) on top of our robot after its first jump. After the load was removed, the robot resumed jumping with negligible degradation of performance (Figure 5B, Movie S13, Supporting Information), surpassing the performance of cockroaches which can withstand forces up to 900× body weight.[71] In addition, for insect-scale robots, a small amount of contaminants attached to its body can add significant weight undermining its mobility. For an optically actuated system, contaminants can further block the incoming light and decrease the photothermal efficiency. Our jumper exhibits a self-cleaning property, preventing contaminants from accumulating on the LCE/Dragon Skin actuator. Using salt particles (feature size: 0.2 – 1.0 mm) sprinkled over the top of the LCE, our robot was able to eject the representative environmental contaminants from its surface with its rapid snap-through motion (Figure 5C).

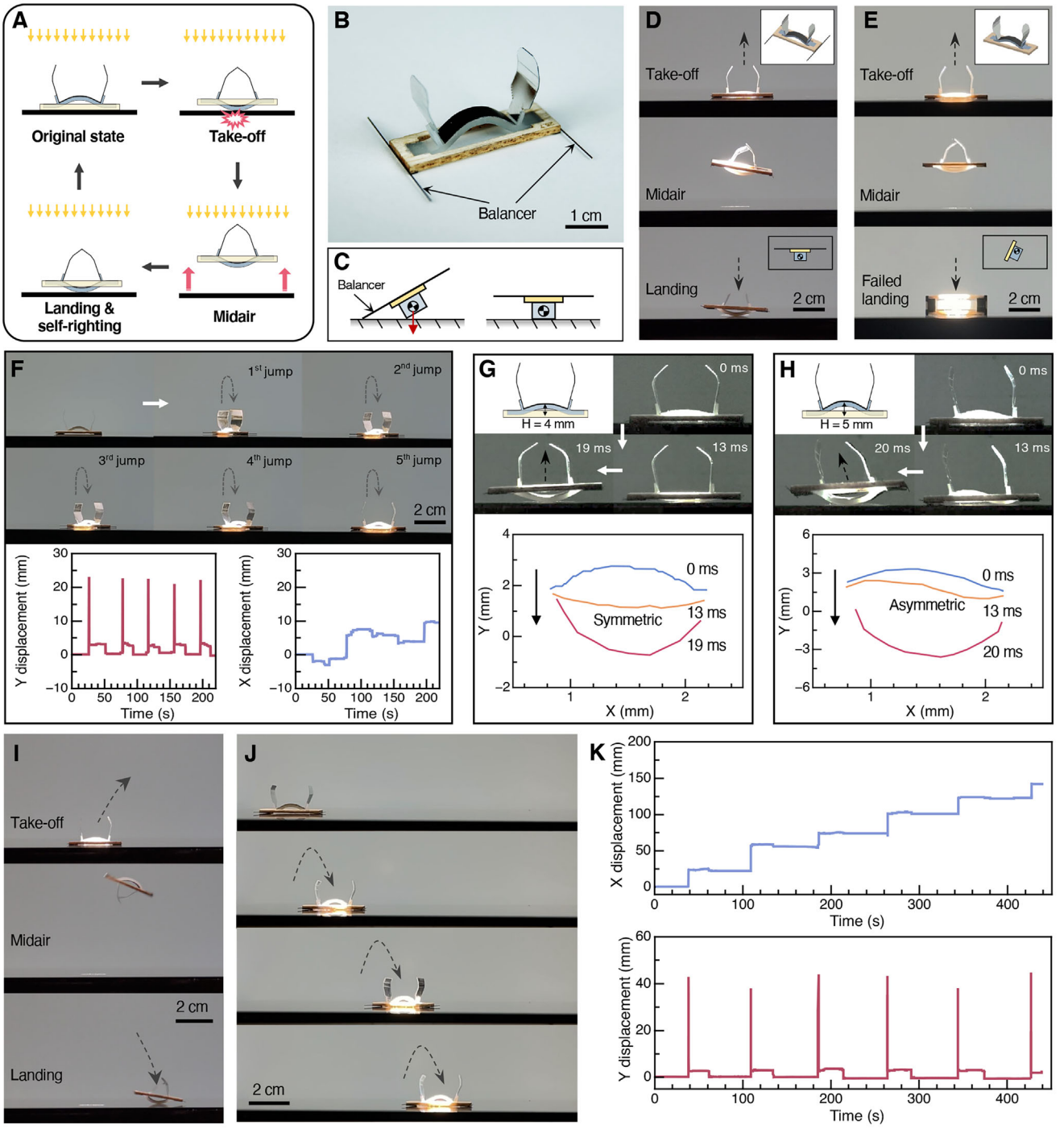

Figure 4. Autonomous, repetitive jumping behavior with a constant visible light. (A) Schematic of a jumper built upon the SSRS mechanism. The snap-though motion provides the impulse to launch the robot. (B) Optical image of a jumping robot that is composed of two balancers attached onto the base of a SSRS device. (C) The balancers function as a passive self-righting mechanism to push the robot upright after landing. A jumper with balancers in. (D) successfully landed while the other without balancers in (E) failed. (F) Snapshots and displacement profiles of a jumping robot in a series of consecutive jumps. (G) Take-off of the robot shown in (D) ($H = 4.0$ mm, $d = 1.3$ mm, light intensity $I = 928$ mW cm^{-2}). Top: key image frames; bottom: shape evolution of the curved beam. The beam has a symmetric transition mode during snap-through, leading to a vertical jump shown in (D and F). (H) Take off of a robot with a deeper beam ($H = 5.0$ mm, $d = 1.3$ mm, $I = 928$ mW cm^{-2}). The beam shows an asymmetric transition, changing the launching angle thus resulting in a directional jump (I). (J and K) Snapshots and displacement of a series of directional consecutive jumps of the robot in (H and I). Note that we moved the light spot to follow the movement of the robot due to its limited size (see Materials and Methods). A large light spot can eliminate this requirement.

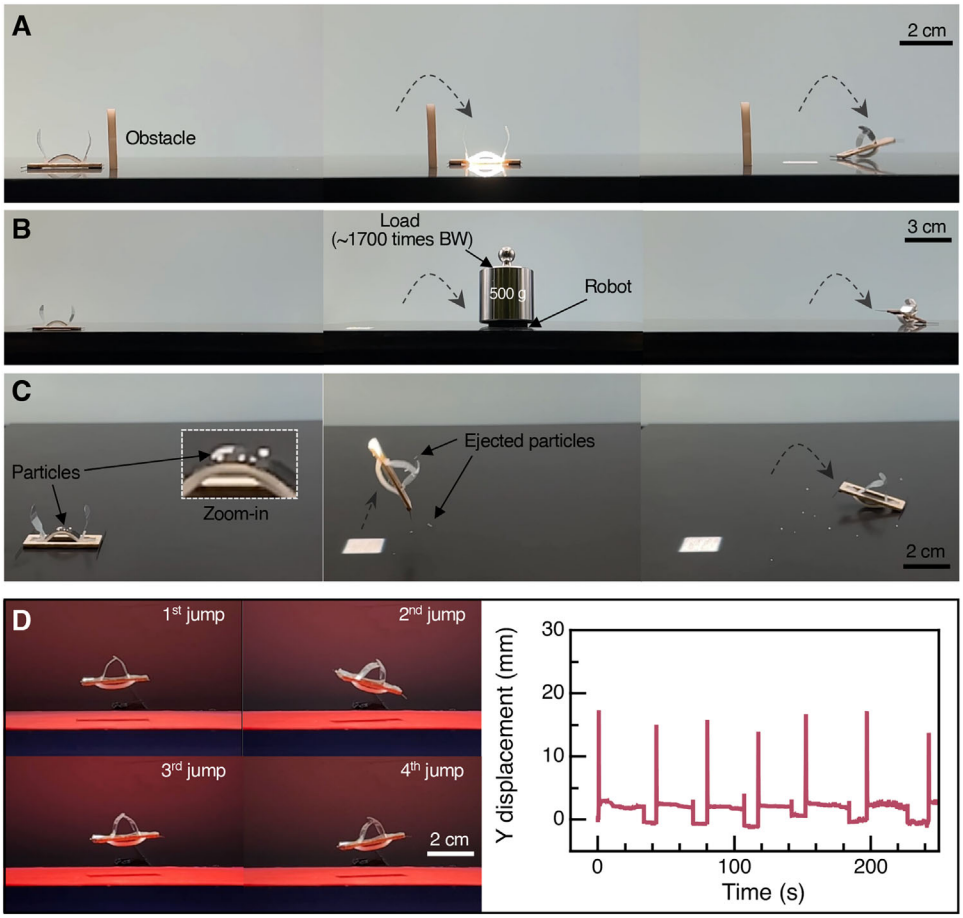

Figure 5. Functional capability of jumping robots. A) The robot is able to jump over a hurdle of 26 mm and continuously locomote afterward. B) The robot resumes its directional jumping after surviving a short-term load of 1700x its own body weight (labeled as BW in the figure). C) The jumping robot possesses a self-cleaning capability, ejecting contaminants (feature size: 0.2 – 1.0 mm) on top of its surface due to the high-speed motion of snapping. Here we used small salt particles to represent contaminants for easy demonstration. The jumping direction and height might be affected by the contaminants. D) Key image frames (left) and vertical displacement curve (right) of continuous jumping under concentrated sunlight. A Fresnel lens was used to concentrate natural. sunlight to create a focused light field of an approximately 15 cm × 15 cm square and of ~1270 mW cm^{-2} light intensity.

For finer particles such as corn starch (feature size: 14 μm), the snap-through motion does not eject all particles, but as long as the LCE receives sufficient light intensity, the continuous snap-through would persist even if the robot is partially covered by the contaminants. (Movie S14, Supporting Information).

To demonstrate that our jumper can continuously harvest solar energy and realize autonomous locomotion in more practical settings, we used a Fresnel lens to concentrate sunlight, forming a focused light field of approximately 15 cm × 15 cm. Also, a cold plate at 18 °C was used to facilitate the cooling of the robot to complete the snap-back process at an ambient temperature of 28 °C. Our robot exhibited self-sustained actuation within the light field without human intervention or artificial power (Figure 5D, Movie S15, Supporting Information), demonstrating its potential for applications of untethered actuation powered by natural ambient energy. It is noteworthy that the robot could repeatedly jump without external cooling under lower ambient temperature and better air convection (14 °C, wind speed = 16 km h^{-1}, Movie S17, Supporting Information). However, for usage under broader environmental conditions, it would be helpful to insulate the robot from the ground by, for example, attaching a "leg" to the monostable beam, which performed jumping and recovery motion on a hot plate at 64 °C (Movie S18, Figure S20, Supporting Information). Alternatively, other active cooling methods like thermoelectric devices (e.g., Peltier devices) can be possibly incorporated into our robot in the future, provided that an onboard power source is available, which could potentially be a triboelectric nanogenerator[72,73] that harvests kinetic energy from the snap-through motion. Environmental factors, e.g., light intensity, spot size, and irradiation angle significantly influence the actuation dynamics of the SSRS-based robot. We found that increasing light intensity leads to a shorter actuation time with minimal effect on jumping height, indicating that the released energy and output power remain nearly constant (Figure S21A, Supporting Information). This observation aligns with our previous conclusion that the released energy of a SSRS device is dominated by the structural instability of the monostable beam rather than the energy input. Additionally, the size of the light spot plays

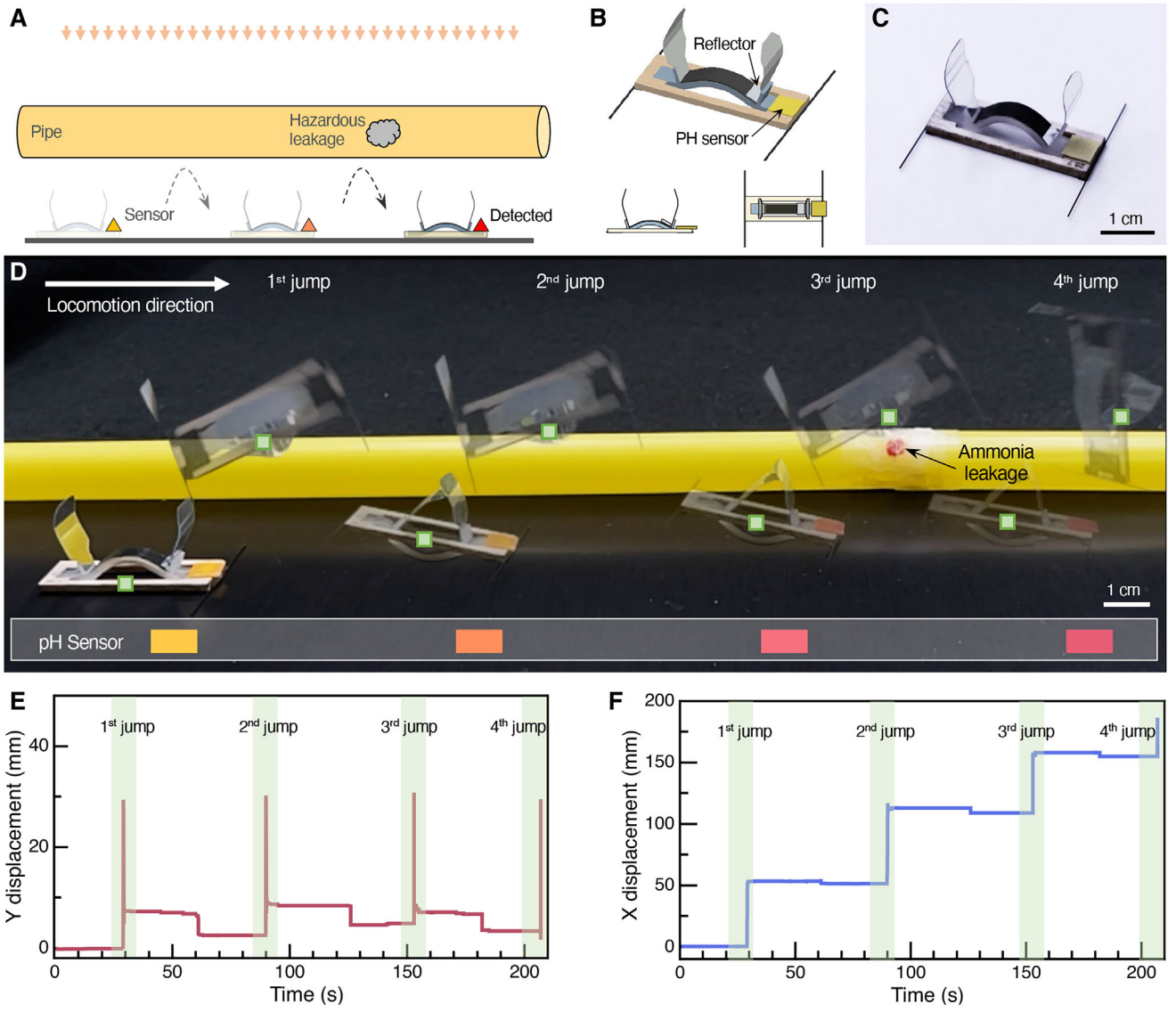

Figure 6. Jumping robot for detection of hazardous gas leakage. (A) Scenario sketch using our insect-scale jumping as a platform for hazardous gas leakage detection. (B and C) A schematic and optical image, respectively, of the jumping robot (~315 mg) equipped with a reflector (negligible mass) and a pH sensor (damp, ~8 mg). The reflector can be used to manipulate the direction and angle of take-off. (D) Time lapse image of the directional jumping robot. The robot performs rightward locomotion toward the leakage location under simulated sunlight. (1020 mW cm^{-2}). The pH test paper gradually turns red from yellow as the robot approaches the ammonia leakage during the process of 4 jumps. (E and F) Displacement of the jumping robot during the gas detection task.

a critical role. When the spot is larger than the LCE film, jumping performance remains consistent; however, as the spot size decreases, the time to jump increases (Figure S21B, Supporting Information). This is because the LCE film requires more time to reach the critical temperature needed to activate the monostable snap-through mechanism. Below a threshold spot diameter (0.9 cm for our test sample), jumping is no longer triggered. Furthermore, we examined the effect of the irradiation zenith angle. As the incident angle becomes more oblique, jumping height slightly decreases and actuation time increases. This behavior is attributed to partial shading by the shutter, which causes uneven and inefficient heating of the LCE film (Figure S21C, Supporting Information).

Insect-scale robots with untethered, autonomous actuation are highly useful for executing tasks in hard-to-reach and harmful environments. We demonstrate that our jumping robot can form the basis for a multifunctional platform capable of remote powering and control for hazardous gas detection with the addition of an onboard sensor. We simulated the scenario of a hazardous gas leakage by drilling an orifice on a plastic tube and injecting a few drops of volatile ammonia hydroxide solution into the tube (**Figure 6A**). We affixed a piece of damp pH test paper onto the frame of a jumper with $H = 5.0$ mm and $d = 1.3$ mm (Figure 6B,C), initially positioned ~138 mm away from the leakage point. Similarly, we only needed a solar simulator to provide steady overhead illumination. To enhance the controllability of

the jumping motion, an optical reflector was attached on the surface of LCE (Figure 6B,C). This reflector can introduce asymmetry by partially covering the LCE, manipulating the jumping direction by enforcing the direction of the snap-through transition mode. In this design, the reflector forced the monostable beam to snap-through with its left part colliding with the ground, propelling the robot rightward. This reflector can also tune the take-off angle after the fabrication of the robot: here, we used this reflector to lower the launching angle to trade off jump height for an increased horizontal locomotion speed. Upon irradiation, it consistently moved in the intended rightward direction. As the jumper approached the orifice, the pH test strip successfully detected the ammonia gas released from the leakage point, leading to its color change from yellow to red (Figure 6D, Movie S16, Supporting Information). A total of four jumps were recorded in the gas detection process, traversing a net distance of 185 mm within 208 seconds with an average jumping height of approximately 30 mm (Figure 6E,F).

3. Discussion

In this work, we have created a class of fully autonomous insect-scale soft robots capable of continuous jumping with energy harvested from the environment, enabled by self-sustained, repeating snapping (SSRS). We have captured physical principles that provide a general guideline for designing snapping-based buckled-beam structures and built-in feedback mechanisms driven by constant environmental light, for the development of repeatable, ballistic motion. Atop this SSRS mechanism, we have developed sub-gram soft robots by incorporating passive self-righting structures to enable autonomous continuous jumping. Owing to their self-sustainability in both energy and motion, these robots can function indefinitely under constant incident light. This was demonstrated by 188 continuous jumps in a single session (and over 800 lifetime jumps), indicating their capability for persistent operation. These robots are also able to jump directionally over a long distance, autonomously detect hazardous gas leakage, avoid an obstacle, and self-clean contaminants. In addition, they are sufficiently robust to survive a short-term load approximately 1700 times its own weight. These capabilities demonstrate the promise for the proposed robots to be deployed into real-world confined environments inaccessible to human or traditional mobile robots (Figure S1, Table S1, Supporting Information).

We envision that our robot could perform more complex sensing tasks by installing lightweight, wireless onboard sensors. To validate its capability of loading these functional components, we tested its jumping performance when subjected to weight loads. Our results show that even at 120 mg of weight load (about 40% of body weight), the robot still achieves approximately 75% of its jumping height without extra load, demonstrating its capability to carry additional functional modules like sensors (see Figure S22, Supporting Information). For example, microscale colorimetric sensors weighing a few milligrams can be used to detect pH, UV, heavy metals, and VOCs, whose image-based readout could be obtained remotely with a camera.[74,75] In addition, a 30 mg battery-free wireless sensor was previously reported to sense light, temperature, and humidity with backscatter communication that enables remote data transmission.[76] An even more sophisticated example features an 84 mg wireless, power-autonomous camera system that streams "first person" monochrome video to a Bluetooth radio from up to 120 m away, which could be mounted on living beetles.[77] Building on this potential for sensing integration, the broader implications of our work extend beyond robotics and span diverse interdisciplinary applications. In environmental monitoring, these robots – equipped with onboard sensors – can autonomously gather data from remote or hazardous locations, aiding early detection of ecological disturbances. For disaster recovery, their agility and compact design facilitate efficient navigation through confined or dangerous spaces, enhancing search and rescue efforts.

Moreover, the low cost of the robot supports large-scale deployment, making it an attractive solution for applications that demand distributed sensing and autonomy. Our platform uniquely integrates energy harvesting, self-regulation, and impulsive actuation through the interplay between photothermal materials and mechanical instability, enabling continuous, high-power motion without external control and establishing a new paradigm for autonomous soft robotics. Future advances in material systems, structural design, and embedded computation will further enhance the robot's capabilities, supporting practical deployment and broader societal impact.

This work advances the field of autonomous, continuous jumping robots. Further exploration on alternative instability mechanisms and photo-active actuators can serve to enhance the robots' performance, improving jumping height, snapping frequency, and locomotion speed. For example, replacing our buckled beams with dome-shaped monostable caps can significantly enlarge the energy density of the system[52] within a suitable integrated design. Alternative optimization targets include lowering the required light intensity to allow a jumper to work directly under natural sunlight.[34] In this work, we demonstrated using light as an environmental stimulus to power the photothermal actuation of LCE; we expect that our strategy can be expanded to materials with other driving mechanisms, such as humidity-driven swelling/deswelling, to broaden the range of conditions and timescales where these strategies can be employed. Other interested environmental stimuli include temperature and magnetic fields. Besides passive strategies demonstrated in this work, active methods to control the jumping direction can greatly enhance the maneuverability. For example, legs with LCEs as activating tendons can actively adjust the launching angle for diverse jumping trajectories. By integrating new building blocks, e.g., sensing and computation components, into our framework, we can further expand their behavioral envelope to realize wider deployment into real-life applications. Ultimately, we have provided a framework to realize self-powered, autonomous high-speed long-lived motion in insect-scale soft robots.

4. Experimental Section

Chemicals: 2-Methyl-1,4-phenylene bis(4-(3-(acryloyloxy)propoxy) benzoate) (RM257), and 2-methyl-1,4- phenylene bis(4-((6(acryloyloxy)hexyl)oxy)benzoate) (RM82) were obtained from Shijiazhuang Sdyano Fine Chemical. 1,3,5-Triallyl-1,3,5-triazine-2,4,6(1H,3H,5H)-trione (TATATO), pentaerythritol tetrakis(3-mercaptopropionate) (PETMP), 2-benzyl-2-(dimethylamino)-4′-morpholinobutyrophenone (Irgacure 369), and butylated hydroxytoluene (BHT) were obtained from Sigma–Aldrich.

Ethylene glycol bis(3-mercaptopropionate) (GDMP) was obtained from TCI. Triethylamine (TEA) was obtained from Merck. All reagents were used as received without further purification.

Synthesis of LCE: Candle soot (CS) was used as the photothermal agent here. It was deposited onto an aluminum foil by clamping the foil above the flame of a paraffin candle and then scraped off from the foil. CS was used without further treatment. The LCE was synthesized using a two-step thiol–ene click reaction.[63] Specifically, 856 mg of RM82, 250 mg of RM257, and 24 mg of BHT were heated to melt in a glass vial at 80 °C. Then, 103 mg of PETMP, 70 mg of TATATO, 404 mg of GDMP, 20 mg of Irgacure 369, and 8.5 mg of CS were added to the melt and magnetically stirred. CS was dispersed using probe sonication at 80 °C for 2 min. About 25 µL of TEA was thoroughly mixed with the solution. The mixture was cast between two Scotch Magic tapecovered glass slides with two layers of labeling tapes (thickness about 280 µm) adhered on the sides as spacers. The glass cell was held at 60 °C for 3.5 h to complete oligomerization, and partially crosslinked LCE film was released from the cell using hot water. The LCE film was uniaxially stretched to 80% strain and photocrosslinked under a UV lamp (UVGO, 365 nm) at an intensity of 35 mW cm^{-2} for 20 mins on each side.

Characterization of Materials: Dynamic mechanical analysis (DMA) of LCE and Dragon Skin was performed by using an analyzer (DMA850, TA Instruments) to test the dynamic moduli and actuation strain of LCE. Rectangular samples with dimension of 25 mm × 4 mm × 0.13 mm were used, which were heated at 150 °C for 5 min prior to testing and allowed to cool to room temperature. A small preload of 0.01 MPa was applied to keep the samples taut. For dynamic moduli measurements, the samples were cycled at an oscillation strain of 0.2% at 1 Hz from 25 to 170 °C with a ramp rate of 5 °C min^{-1}. Actuation strain was tested from 25 to 170 °C with a ramp rate of 5 °C min^{-1}. Cycling test of actuation strain of LCE was performed equilibrating the LCE strip (25 mm × 4 mm × 0.13 mm) at 25 °C and 100 °C in sequence, and a total of 10 cycles were tested. Optical images was taken using a digital camera (EOS 70D, Canon) and the length was analyzed using Tracker software. To measure the nematic-to-isotropic transition temperature of LCE, differential scanning calorimetry (DSC) of LCE was performed using DSC250 from TA Instruments. Approximately 10 mg of sample was added to an aluminum pan. All samples were heated to 180 °C at 10 °C min^{-1} and held isothermally for 2 min to erase the thermal history. Then, the samples were cooled to 0 °C at 20 °C min^{-1}, held isothermally for 2 min, and heated to 180 °C at 10 °C min^{-1}. UV-Vis spectrum of LCE was measured to investigate the absorption properties using UV-3101 PC from Shimadzu.

Fabrication of SSRS and Jumping Robot: The fabrication flow of the SSRS device and jumping robot is illustrated in Figure S23 (Supporting Information). Photocurable resin molds were printed using a 3D printer (Form 3, Formlabs). Dragon Skin 30 was cast into the molds, degassed under vacuum, and allowed to cure for 24 h. The Dragon Skin elastomer beam was released from the mold with extra material removed with a razor blade (Figure S24, Supporting Information). Silicone adhesive (500°F RTV High Heat Silicone Sealant, Rutland) dissolved in hexanes (50 w/v%) was used to glue the LCE and elastomer beam. A balsa wood frame (1.5 mm thick, Qj-solar) was cut using laser cutting (Speedy 300 Flexx, Trotec Laser Inc.). Two small pieces of carbon fiber substrate, the wooden frame, the LCE/elastomer beam bilayer, and two PET shutters (DuraLar, Grafix Plastics) were assembled using super glue. For self-righting jumping robots, two pieces of carbon fiber (30 mm long, 0.26 mm diameter) were attached to the sides of the wooden frame using super glue.

Actuation of SSRS Device and Jumping Robot: A solar simulator (HAL-320 W, Asahi Spectra) was used to irradiate a SSRS device or a robot from an overhead direction (Figure S25A, Supporting Information). For actuation of jumping robots, the light source is moved horizontally on a customized supporting rig to track the position of the jumping robot after each jump while maintaining the light intensity. This tracking is solely to compensate the light spot's limited size; a larger light spot would negate this necessity. For actuation under concentrated sunlight, a Fresnel lens (Greenpower science, 74 cm × 51 cm) was used to yield a light field of approximately 15 cm in diameter. The jumping robot was placed on top of a cool plate (Figure S25B, Supporting Information). We used a chiller (Heidorph, RotaChill Large) to maintain the temperature of a cold plate at 18 °C to speed up the reset of the robot by enhancing the cooling process. This sunlight actuation experiment was conducted at ≈13:00pm on July 19, 2023 in sunny weather conditions in Los Angeles (latitude of 34° North, longitude of 118° West). Ambient temperature was 28 °C and there was no wind.

Characterization of SSRS Device and Jumping Robot: The motion of a SSRS device and jumping robot was recorded using a high speed camera (VEO-710L, Phantom). The trajectories were then analyzed using the software, Tracker (version 5.0.5). Infrared videos of SSRS devices/jumping robots were obtained using an infrared camera (TiX 580, Fluke). The method of extracting the corresponding temperature curves from the infrared videos are detailed in Text S7 (Supporting Information). Characterization of the released energy and output power are adapted from ref. [78], which are detailed in Texts S4 and S5 (Supporting Information), respectively.

Supporting Information

Supporting Information is available from the Wiley Online Library or from the author.

Acknowledgements

The authors acknowledge ONR awards N000141812314, N000142412187, and N000142212595 received by X.H. This project received partial support from the ONR (Office of Naval Research) under grant N000142212449 and the DARPA (Defense Advanced Research Projects Agency) grant D22AP00136 received by A.M. W.Y. acknowledges support from startup funds provided by the Department of Mechanical and Aerospace Engineering, University of California, Davis. The authors also thank Dr. R. Wood for the insightful discussion.

Conflict of Interest

The authors declare no conflict of interest.

Author Contributions

W.Y. and P.S. contributed equally to this work. P.S., W.Y., and X.H. conceived the concept and planned the project; Y.Z., P.S., Y.Y., and C.C. developed LCE actuators and conducted characterization; Z.L. developed finite element simulation; Y.C. applied their previously developed buckling theory; W.Y. and P.S. designed and performed the fabrication and characterization of SSRS devices; W.Y., P.S, and D.M. prepared figures and drafted the manuscript; all authors revised the manuscript; A.M. supported W.Y.; X.H. supervised the research and supported with material fabrication, characterization, and testing platforms.

Data Availability Statement

The data that support the findings of this study are available in the supplementary material of this article.

Keywords

autonomous robot, liquid crystal elastomer, nature-inspired machine, self-sustained locomotion, soft robot

Received: October 6, 2025
Revised: November 3, 2025
Published online:

[1] J. C. Tuthill, R. I. Wilson, *Curr. Biol.* **2016**, *26*, R1022.
[2] A. Biewener, S. Patek, *Animal Locomotion*, Oxford University Press, United Kingdom, **2018**.
[3] R. St. Pierre, S. Bergbreiter, *Annu.Rev. Control Robot. Auton. Syst.* **2019**, *2*, 231.
[4] Y. Wang, Q. Wang, M. Liu, Y. Qin, L. Cheng, O. Bolmin, M. Alleyne, A. Wissa, R. H. Baughman, D. Vella, S. Tawfick, *Proc. Natl. Acad. Sci U.S.A.* **2023**, *120*, 2210651120.
[5] P. Rothemund, Y. Kim, R. H. Heisser, X. Zhao, R. F. Shepherd, C. Keplinger, *Nat. Mater.* **2021**, *20*, 1582.
[6] N. T. Jafferis, E. F. Helbling, M. Karpelson, R. J. Wood, *Nature* **2019**, *570*, 491.
[7] S. Hollar, A. Flynn, C. Bellew, K. Pister, *The Sixteenth Annual International Conference on Micro Electro Mechanical Systems, MEMS- 03 Kyoto*, (IEEE, New York City, **2003**), pp. 706–711.
[8] S. Bergbreiter, K. S. Pister, *Proceedings 2007 IEEE International Conference on Robotics and Automation*, (IEEE, New York City, **2007**), pp. 447–453.
[9] W. Hu, G. Z. Lum, M. Mastrangeli, M. Sitti, *Nature* **2018**, *554*, 81.
[10] V. M. Ortega-Jimenez, E. J. Challita, B. Kim, H. Ko, M. Gwon, J.-S. Koh, M. S. Bhamla, *Proc. Natl. Acad. Sci. U.S.A.* **2022**, *119*, 2211283119.
[11] J. T. Greenspun, K. Pister, *Hilton Head Solid-State Sensors, Actuators, and Microsystems Workshop*, Hilton Head Island, SC **2018**, Vol. *3*.
[12] W. A. Churaman, L. J. Currano, C. J. Morris, J. E. Rajkowski, S. Bergbreiter, *J. Microelectromechanical Syst.* **2011**, *21*, 198.
[13] Y. Sun, J. Wang, C. Sung, *2022 International Conference on Robotics and Automation (ICRA)*, (IEEE, New York City **2022**), pp. 7189.
[14] D. W. Haldane, M. M. Plecnik, J. K. Yim, R. S. Fearing, *Sci. Robot.* **2016**, *1*, aag2048.
[15] N. W. Bartlett, M. T. Tolley, J. T. Overvelde, J. C. Weaver, B. Mosadegh, K. Bertoldi, G. M. Whitesides, R. J. Wood, *Science* **2015**, *349*, 161 .
[16] E. W. Hawkes, C. Xiao, R.-A. Peloquin, C. Keeley, M. R. Begley, M. T. Pope, G. Niemeyer, *Nature* **2022**, *604*, 657.
[17] R. Armour, K. Paskins, A. Bowyer, J. Vincent, W. Megill, *Bioinspir. Biomim.* **2007**, *2*, S65.
[18] Y. Chi, Y. Zhao, Y. Hong, Y. Li, J. Yin, *Adv. Intell. Syst.* **2023**, 2300063.
[19] J.-S. Koh, E. Yang, G.-P. Jung, S.-P. Jung, J. H. Son, S.-I. Lee, P. G. Jablonski, R. J. Wood, H.-Y. Kim, K.-J. Cho, *Science* **2015**, *349*, 517.
[20] R. Chen, Z. Yuan, J. Guo, L. Bai, X. Zhu, F. Liu, H. Pu, L. Xin, Y. Peng, J. Luo, S. Tang, Q. Lu, X. Wang, H. Wang, G. Chen, *Nat. Commun.* **2021**, *12*, 7028 .
[21] M. Duduta, F. Berlinger, R. Nagpal, D. R. Clarke, R. J. Wood, F. Z. Temel, *IEEE Robot. Autom. Lett.* **2020**, *5*, 3868.
[22] Y. Wu, J. K. Yim, J. Liang, Z. Shao, M. Qi, J. Zhong, Z. Luo, X. Yan, M. Zhang, X. Wang, R. S. Fearing, R. J. Full, L. Lin, *Sci. Robot.* **2019**, *4*, aax1594.
[23] Q. Wang, X. Tian, D. Li, *Smart Mater. Struct.* **2021**, *30*, 085038.
[24] G.-Z. Yang, J. Bellingham, P. E. Dupont, P. Fischer, L. Floridi, R. Full, N. Jacobstein, V. Kumar, M. McNutt, R. Merrifield, B. J. Nelson, B. Scassellati, M. Taddeo, R. Taylor, M. Veloso, Z. L. Wang, R. Wood, *Sci. Robot.* **2018**, *3*, aar7650.
[25] R. L. Truby, S. Li, *Sci. Robot.* **2020**, *5*, abd7338.
[26] M. Sitti, *Extreme Mech. Lett.* **2021**, *46*, 101340.
[27] W. Yan, A. Mehta, *Soft Robot* **2022**, *9*, 871.
[28] Y. Zhao, Y. Chi, Y. Hong, Y. Li, S. Yang, J. Yin, *Proc. Natl. Acad. Sci. U.S.A.* **2022**, *119*, 2200265119.
[29] W. Yan, S. Li, M. Deguchi, Z. Zheng, D. Rus, A. Mehta, *Nat. Commun.* **2023**, *14*, 1553.
[30] D. Ge, K. Li, *Int. J. Mech. Sci.* **2022**, *233*, 107646.
[31] P. Xu, J. Jin, K. Li, *Int. J. Mech. Sci.* **2021**, *208*, 106686.
[32] C. Chen, X. Zhao, Y. Chen, W. Chu, Y. Wu, Y. Zhao, P. Shi, W. Chen, H. Li, X. He, H. Liu, *Nano Lett.* **2022**, *22*, 8413.
[33] L. Qin, X. Liu, Y. Yu, *Adv. Opt. Mater.* **2021**, *9*, 2001743.
[34] Y. Zhao, Q. Li, Z. Liu, Y. Alsaid, P. Shi, M. K. Jawed, X. He, *Sci. Robot.* **2023**, *8*, adf4753.
[35] C. Ahn, K. Li, S. Cai, *ACS Appl. Mater. Interfaces* **2018**, *10*, 25689.
[36] A. H. Gelebart, D. J. Mulder, M. Varga, A. Konya, G. Vantomme, E. Meijer, R. L. Selinger, D. J. Broer, *Nature* **2017**, *546*, 632.
[37] K. Korner, A. S. Kuenstler, R. C. Hayward, B. Audoly, K. Bhattacharya, *Proc. Natl. Acad. Sci. U.S.A.* **2020**, *117*, 9762.
[38] A. Fernandes Minori, S. Jadhav, H. Chen, S. Fong, M. T. Tolley, *Front. Robot. AI* **2022**, *9*, 844282.
[39] S. Longo, S. Cox, E. Azizi, M. Ilton, J. Olberding, R. S. Pierre, S. Patek, *J. Exp. Biol.* **2019**, *222*, jeb197889.
[40] M. Ilton, M. S. Bhamla, X. Ma, S. M. Cox, L. L. Fitchett, Y. Kim, J.-S. Koh, D. Krishnamurthy, C.-Y. Kuo, F. Z. Temel, A. J. Crosby, M. Prakash, G. P. Sutton, R. J. Wood, E. Azizi, S. Bergbreiter, S. N. Patek, *Science* **2018**, *360*, aao1082.
[41] E. Steinhardt, N.-s. P. Hyun, J.-s. Koh, G. Freeburn, M. H. Rosen, F. Z. Temel, S. Patek, R. J. Wood, *Proc. Natl. Acad. Sci. U.S.A.* **2021**, *118*, 2026833118.
[42] J. Hu, Z. Nie, M. Wang, Z. Liu, S. Huang, H. Yang, *Angew. Chem., Int. Ed.* **2023**, *62*, 202218227.
[43] J. Jeon, J.-C. Choi, H. Lee, W. Cho, K. Lee, J. G. Kim, J.-W. Lee, K.-I. Joo, M. Cho, H.-R. Kim, J. J. Wie, *Mater. Today* **2021**, *49*, 97.
[44] W. Yan, Y. Yu, A. Mehta, *Theor. App. Mech. Lett.* **2019**, *9*, 264.
[45] W. Yan, A. L. Gao, Y. Yu, A. Mehta, *International Symposium on Experimental Robotics*, IFRR, San Francisco, Montreal, **2018**, pp. 631–644.
[46] M. Mungekar, L. Ma, W. Yan, V. Kackar, S. Shokrzadeh, M. K. Jawed, *Adv. Mater. Technol.* **2023**, *8*, 2300088.
[47] W. Yan, C. Liu, A. Mehta, *2021 IEEE/RSJ International Conference on Intelligent Robots and Systems*, IEEE/RSJ, Pittsburgh, Pennsylvania, USA, **2021**, pp. 6084–6089.
[48] B. Gorissen, D. Melancon, N. Vasios, M. Torbati, K. Bertoldi, *Sci. Robot.* **2020**, *5*, abb1967.
[49] T. Chen, O. R. Bilal, K. Shea, C. Daraio, *Proc. Natl. Acad. Sci. U.S.A.* **2018**, *115*, 5698.
[50] J. Wang, T. Zhao, Y. Fan, H. Wu, J.-a. Lv, *Adv. Funct. Mater.* **2023**, *33*, 2209798.
[51] H. Guo, A. Priimagi, H. Zeng, *Adv. Funct. Mater.* **2022**, *32*, 2108919.
[52] Y. Kim, J. van den Berg, A. J. Crosby, *Nat. Mater.* **2021**, *20*, 1695.
[53] G. Graeber, K. Regulagadda, P. Hodel, C. Küttel, D. Landolf, T. M. Schutzius, D. Poulikakos, *Nat. Commun.* **2021**, *12*, 1727 .
[54] T. S. Hebner, K. Korner, C. N. Bowman, K. Bhattacharya, T. J. White, *Sci. Adv.* **2023**, *9*, ade1320.
[55] X. Zhou, G. Chen, B. Jin, H. Feng, Z. Chen, M. Fang, B. Yang, R. Xiao, T. Xie, N. Zheng, *Adv Sci.* **2024**, *11*, 2402358.
[56] F. Qi, C. Zhou, H. Qing, H. Sun, J. Yin, *arXiv preprint* **2025**.
[57] X. Qian, Y. Zhao, Y. Alsaid, X. Wang, M. Hua, T. Galy, H. Gopalakrishna, Y. Yang, J. Cui, N. Liu, M. Marszewski, L. Pilon, H. Jiang, X. He, *Nat. Nanotechnol.* **2019**, *14*, 1048.
[58] Y. Zhao, C. Xuan, X. Qian, Y. Alsaid, M. Hua, L. Jin, X. He, *Sci. Robot.* **2019**, *4*, aax7112.
[59] M. Hua, C. Kim, Y. Du, D. Wu, R. Bai, X. He, *Matter* **2021**, *4*, 1029 .
[60] Y. Yan, Y. Zhao, Y. Alsaid, B. Yao, Y. Zhang, S. Wu, X. He, *Adv. Intell. Syst.* **2021**, *3*, 2000234.
[61] X. He, M. Aizenberg, O. Kuksenok, L. D. Zarzar, A. Shastri, A. C. Balazs, J. Aizen- berg, *Nature* **2012**, *487*, 214 .
[62] C. Chen, P. Shi, Z. Liu, S. Duan, M. Si, C. Zhang, Y. Du, Y. Yan, T. J. White, R. Kramer-Bottiglio, M. Sitti, T. Iwasaki, X. He, *Sci. Rob.* **2025**, *10*, ads1292.
[63] M. O. Saed, C. P. Ambulo, H. Kim, R. De, V. Raval, K. Searles, D. A. Siddiqui, J. M. O. Cue, M. C. Stefan, M. R. Shankar, *Adv. Funct. Mater.* **2019**, *29*, 1806412 .
[64] P. Shi, Y. Zhao, Z. Liu, X. He, *J. Compos. Mater.* **2023**, *57*, 633.
[65] Y. Chen, T. Liu, L. Jin, *Adv. Intell. Syst.* **2022**, *4*, 2100270.

[66] N. J. Kotlarewski, B. Belleville, B. K. Gusamo, B. Ozarska, *Eur. J. Wood Wood Prod.* **2016**, *74*, 83.
[67] N. Vahedi, C. Tiago, A. P. Vassilopoulos, J. R. Correia, T. Keller, *Constr. Build. Mater.* **2022**, *329*, 127164.
[68] H. Bennet-Clark, *J. Exp. Biol.* **1975**, *63*, 53.
[69] M. Kovač, M. Schlegel, J.-C. Zufferey, D. Floreano, *Auton. Robot.* **2010**, *28*, 295.
[70] A. Pandey, D. E. Moulton, D. Vella, D. P. Holmes, *Europhys. Lett.* **2014**, *105*, 24001.
[71] K. Jayaram, R. J. Full, *Proc. Natl. Acad. Sci. U.S.A.* **2016**, *113*, E950.
[72] T. Cheng, J. Shao, Z. L. Wang, *Nat. Rev. Methods Primers* **2023**, *3*, 39.
[73] Q. Bai, X.-W. Liao, Z.-W. Chen, C.-Z. Gan, H.-X. Zou, K.-X. Wei, Z. Gu, X.-J. Zheng, *Nano Energy* **2022**, *96*, 107118.
[74] H.-J. Yoon, G. Lee, J.-T. Kim, J.-Y. Yoo, H. Luan, S. Cheng, S. Kang, H. L. T. Huynh, H. Kim, J. Park, J. Kim, S. S. Kwak, H. Ryu, J. Kim, Y. S. Choi, H.-Y. Ahn, J. Choi, S. Oh, Y. H. Jung, M. Park, W. Bai, Y. Huang, L. P. Chamorro, Y. Park, J. A. Rogers, *Sci. Adv.* **2022**, *8*, ade3201.
[75] M. Qin, M. Sun, R. Bai, Y. Mao, X. Qian, D. Sikka, Y. Zhao, H. J. Qi, Z. Suo, X. He, *Adv, Mater* **2018**, *30*, 1800468.
[76] V. Iyer, H. Gaensbauer, T. L. Daniel, S. Gollakota, *Nature* **2022**, *603*, 427.
[77] V. Iyer, A. Najafi, J. James, S. Fuller, S. Gollakota, *Sci. Rob.* **2020**, *5*, abb0839.
[78] G. Mao, M. Drack, M. Karami-Mosammam, D. Wirthl, T. Stockinger, R. Schwödiauer, M. Kaltenbrunner, *Sci. Adv.* **2020**, *6*, abc0251.
[79] M. R. Shankar, M. L. Smith, V. P. Tondiglia, K. M. Lee, M. E. McConney, D. H. Wang, L.-S. Tan, T. J. White, *Proc. Natl. Acad. Sci. U.S.A.* **2013**, *110*, 18792.